Imaging Resolution of the 410-km and 660-km Discontinuities

Kai Deng

Thesis submitted to the Faculty of the
Virginia Polytechnic Institute and State University
in partial fulfillment of the requirements for the degree of

Master of Science
in
Geosciences

Ying Zhou, Chair
John A. Hole
Scott D. King

August 6, 2014
Blacksburg, Virginia

Keywords: Wave scattering and diffraction, Computational seismology, Theoretical seismology, Wave propagation

Imaging Resolution of 410-km and 660-km Discontinuities

Kai Deng

(ABSTRACT)

The structure of seismic discontinuities at depths of about 410 km and 660 km provides important constraints on mantle convection as the associated mineral phase transformations in the transition zone are sensitive to thermal perturbations. Teleseismic *P-to-S* receiver functions have been widely used to map the depths of the two discontinuities. In this study, we investigate the resolution of receiver functions in imaging topographic variations of the 410-km and 660-km discontinuities based on wave propagation simulations using a Spectral Element Method (SEM). We investigate finite-frequency effects of direct P waves as well as *P-to-S* converted waves by varying the length scale of discontinuity topography in the transition zone. We show that wavefront healing effects are significant in broadband receiver functions. For example, at a period of 10 to 20 seconds, the arrivaltime anomaly in *P-to-S* converted waves is about 50% of what predicted by ray theory when the topography length scale is in the order of 400 km. The observed arrival anomaly further reduces to 10$\sim$20% when the topography length scale reduces to about 200 km. We calculate 2-D boundary sensitivity kernels for direct P waves as well as receiver functions based on surface wave mode summation and confirm that finite frequency-effects can be properly accounted for. Three-dimensional wavespeed structure beneath seismic stations can also introduce significant artifacts in transition zone discontinuity topography if time corrections are not applied, and, the effects are dependent on frequency.

Acknowledgments

I would like to thank first and foremost my advisor, Dr. Ying Zhou, for her continuous guidance and help throughout my research. I am grateful to my committee members, Dr. John A. Hole and Dr. Scott D. King, for their constructive advice and great help on my research.

I wish to thank the staffs in the department of Geosciences, Connie Lowe, Mary McMurray Ellen Mathena, Sharon Collins, Jo Thomason, James R. Dunson, Jim Langridge and Mark Lemon for their kind help in the past two years.

I would like to thank the Advanced Research Computing (ARC) at Virginia Tech for providing computational resources and especially Justin Krometis at ARC for technical support.

Also, I would like to thank the geophysical students in the department of Geosciences for their friendship and help in the past two years.

Contents

List of Figures

Chapter 1

Introduction

Seismic discontinuities in the mantle transition zone at depths of about 410 and 660 km are associated with olivine phase transformations (Birch, 1952). Depths of the discontinuities depend on temperature as well as thermodynamic parameters governing the phase transition. The Clapeyron slope is positive for the 410-km discontinuity and negative for the 660-km discontinuity (Katsura & Ito, 1989; Bina & Helffrich, 1994). Therefore, topographic variations of the two seismic discontinuities can used to infer spatial variations in temperature and provide important constraints on the dynamics of subducting slabs and mantle plumes in the transition zone (e.g., Shearer & Masters, 1992; Flanagan & Shearer, 1998; Li et al., 1998, 2003; Helffrich et al., 2010; Benoit et al., 2013).

Receiver functions which isolate *P-to-S* converted waves from *P* wave coda (Langston, 1979) have been widely used to image lateral variations in transition zone discontinuity depths at both regional and global scales (e.g., Lawrence & Shearer, 2006; Andrews & Deuss, 2008; Leahy, 2009; Long et al., 2010). Migration and stacking techniques (Dueker & Sheehan, 1997; Sheehan et al., 2000) are often used to reduce structural noise assuming that the effects of 3-D wavespeed structure can be averaged out. Several recent seismic array studies applied common conversion point (CCP) stacking of broadband receiver functions to map relatively small-scale discontinuity structure in the transition zone (e.g., Dueker & Sheehan, 1997;

Cao & Levander, 2010; Eagar et al., 2010; Schmandt et al., 2012). Migration and stacking of broader receiver functions in transition zone studies have been based on ray theory, which is a high-frequency approximation and breaks down when the length scale of lateral heterogeneity is comparable to the characteristic wavelength of seismic waves. Finite-frequency effects can be important when it comes to imaging small-scale topographic structures.

The reference wavespeed structure used in migration and stacking also plays an important role in the resolution of receiver functions. Travel time corrections based on local wavespeed structure is necessary when there are mantle wavespeed heterogeneities near stations. Schmandt et al. (2012) made wavespeed corrections based on tomographic models in their study of the 660-km discontinuity using receiver functions and pointed out that correcting for regional P and S tomographic structure could reduce the standard deviation of the 410-km and 660-km discontinuity depths by about 40%. Travel time corrections in ray theory only account for wavespeed structure along ray paths of P and *P-to-S* converted waves (Eagar et al., 2010; Schmandt et al., 2012), delay times of *P-to-S* converted waves caused by wavespeed anomaly may be over-corrected or under-corrected when near-receiver wavespeed structure is small compared to seismic wavelength, leading to biased discontinuity depths.

There has been growing interest in mapping high-resolution transition zone discontinuity topography using finite-frequency sensitivity to boundary perturbations. For example, Lawrence & Shearer (2008) applied finite-frequency boundary sensitivity of Dahlen (2005) to reflected waves (SdS) in the SS precursors and resolved small-scale discontinuity structures. In this study, we exam finite-frequency effects in receiver functions based on wave propagation simulations in 3-D models with lateral variations in discontinuity depths using the Spectral Element Method (Komatitsch & Tromp, 1999, 2002). We adapt the SEM mesh to incorporate topography of the 410-km and 660-km discontinuities. We calculate receiver functions following the standard deconvolution and migration process and investigate limitations of the traditional imaging methods. The SEM receiver function delay times are compared with predictions calculated based upon ray theory. We show that for the 410-km

discontinuity, when the topography length scale is in the order of 200–400 km, travel time anomaly of *P-to-S* receiver function is about 20–50% of what predicted by ray theory at the period of 10 to 20 seconds. Finite-frequency effects are more significant for perturbations in the 660-km discontinuity and the receiver function arrival anomaly is only ∼30% of ray prediction at the same periods when the length scale of the topography is ∼400 km. We calculate 2-D boundary sensitivity kernels for travel times measured between synthetic and observed receiver functions based on surface wave mode summation (Zhou et al., 2005; Zhou, 2009) and show that 2-D finite-frequency boundary sensitivity kernels can be applied to image small-scale topography of transition zone discontinuities.

Effects of anelasticity and discontinuity sharpness are also discussed. We show that physical dispersion caused by anelasticity, if not accounted for, can introduce systematic bias in the 410-km and 660-km discontinuity depths in broadband receiver functions. While we model transition zone discontinuities as first-order discontinuities in SEM simulations, our calculations with models replacing the first-order wavespeed jump by a gradient zone over a finite depth range show that receiver functions in different frequency bands can be potentially used to constrain the "thickness" of the discontinuities.

Finally, we discuss the effects of three-dimensional wavespeed anomalies on receiver function delay times and show that wavespeed corrections based on ray theory can be safely applied in receiver functions at periods shorter than 20 s when the characteristic length scale of wavespeed anomalies exceeds 500 km.

Chapter 2

Seismic Wave Propagation in 3-D Earth Models

We simulate seismic wave propagation in 3-D earth models with lateral variation in discontinuity depths using the Spectral Element Method (Komatitsch & Tromp, 1999, 2002). In SEM simulations, the earth is subdivided into six chunks and each chunk has 640×640 elements at the free surface, and the simulations are accurate down to a period of 7 seconds. A slightly modified PREM (preliminary reference earth model) (Dziewonski & Anderson, 1981) is used as our reference model, which we refer to PREM for the rest of the paper. The actual depths of the two discontinuities are at 400 km and 670 km in the reference model.

In this chapter, we will discuss the implementation of the 410-km and 660-km discontinuity topography in SEM mesh and limitations and accuracy associated with the simulation. P wave and receiver function travel time measurements made on SEM synthetics for a range of transition zone topographic models will be discussed in Chapter 4.

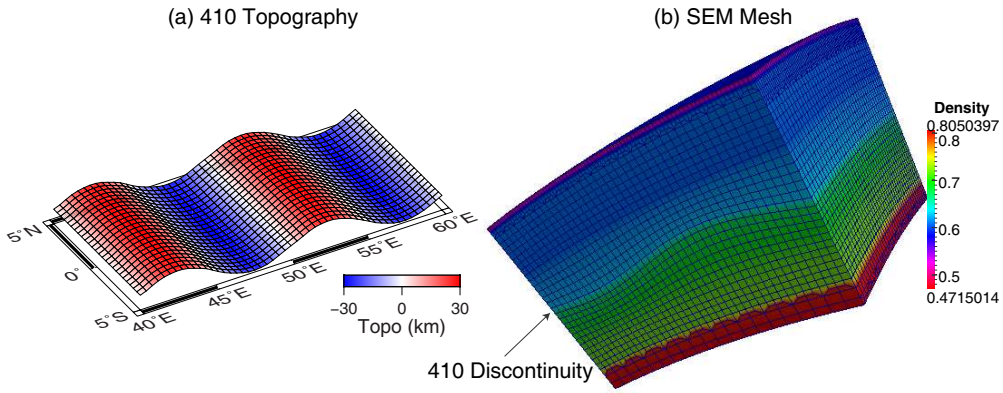

Figure 2.1: Example SEM mesh with a topography on the 410-km discontinuity. The topographic variation has a structure of spherical harmonics and a wavelength of about 1000 km. Left: the 410-km discontinuity topography on a map view; positive for upward deflection and negative for downward deflection. Right: SEM mesh from earth surface to the 660-km discontinuity; the color scale indicates density normalized by the average value of the Earth $\bar{\rho} = 5514.3$ kg/m^3.

2.1 The 410-km Discontinuity in SEM

Fig.2.1 shows an example SEM mesh with a deformed 410-km discontinuity. To incorporate discontinuity topography into the SEM mesh, we extrapolate the wavespeed and density structure between 220 and 400 km in PREM all the way down to 600 km. The spectral elements are then deformed with wavespeed and density between the deformed discontinuity and 600 km depth overwritten by the PREM polynomials for structures below the discontinuity. The meshing preserves the wavespeed gradient in PREM as well as honours the 410-km interface as a first-order discontinuity. To benchmark SEM simulations, we change the depth of the discontinuity from 400 km to 430 km in two different simulations and compare the seismograms. In the first simulation, we only change PREM discontinuity depth in the original SEM code, and in a second simulation, we add a constant perturbation of -30 km to the discontinuity using our meshing scheme as discussed above.

In SEM simulations, the displacement field is represented as Lagrange polynomials with five Gauss-Lobatto-Legendre (GLL) points on each side of an element (Komatitsch & Tromp,

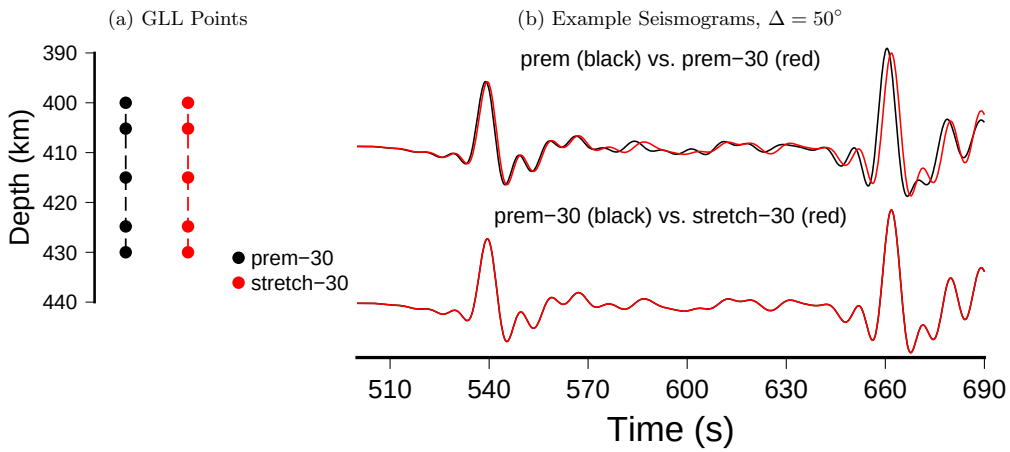

Figure 2.2: (a) Radial GLL points in an element just above the 410-km discontinuity when the discontinuity is moved downward by 30 km. (b) Example vertical-component seismograms. A phase shift between seismograms in the unperturbed model and perturbed model is seen due to depth perturbation of the 410-km discontinuity. The two different approaches of adding a constant perturbation to 410 discontinuity generate identical GLL points and seismograms. The seismograms are for an epicentral distance of 50° and band pass filtered between 50 s and 8 s.

1999). In the benchmark simulations, the two approaches should have identical GLL points for a spherically symmetric perturbation of the 410-km discontinuity (Fig.2.2a). Fig.2.3 shows that the seismograms agree exactly, indicating our new meshing scheme represents topography perturbations faithfully.

In implementing lateral variations of the 410-km discontinuity in SEM, the topography has to be discretized. This introduces numerical noises which depends on the size of the spectral elements. For the meshing parameters we use (640×640×6 elements at free surface), we have done benchmark simulations with decreased mesh size to confirm that topographic variations with a length scale greater than 2° can be modeled with high accuracy. For shorter length scale perturbation, the number of GLL points becomes insufficient to capture topographic variations (Fig.2.4).

Fig.2.5 shows example radial-component seismograms and receiver functions in an earth model with lateral variations in the 410-km discontinuity depth. The topography has a

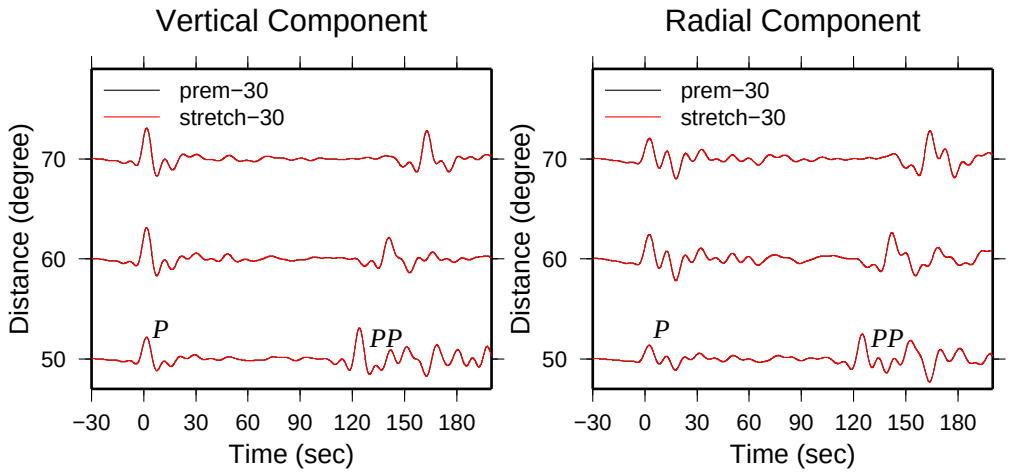

Figure 2.3: Comparison between SEM seismograms generated using the original SEM code (prem-30) and our new mesh (stretch-30). The two approaches generated identical seismograms.

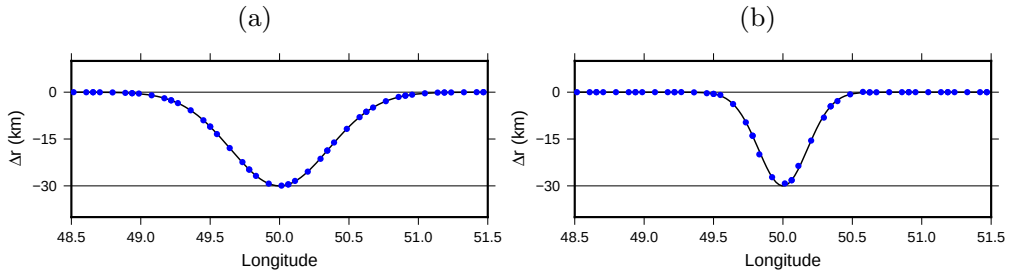

Figure 2.4: Gaussian topography of the 410-km discontinuity (solid lines) and GLL points in SEM (blue dots) representing the topography. The meshing parameter used is 640×640×6 elements at the free surface. A negative Δr indicates a downward deflection of the discontinuity. (a) The width of the Gaussian is about 2°. (b) The width of the Gaussian is about 1°. Numerical noises become an issue when the length scale of the variation is smaller than 2°.

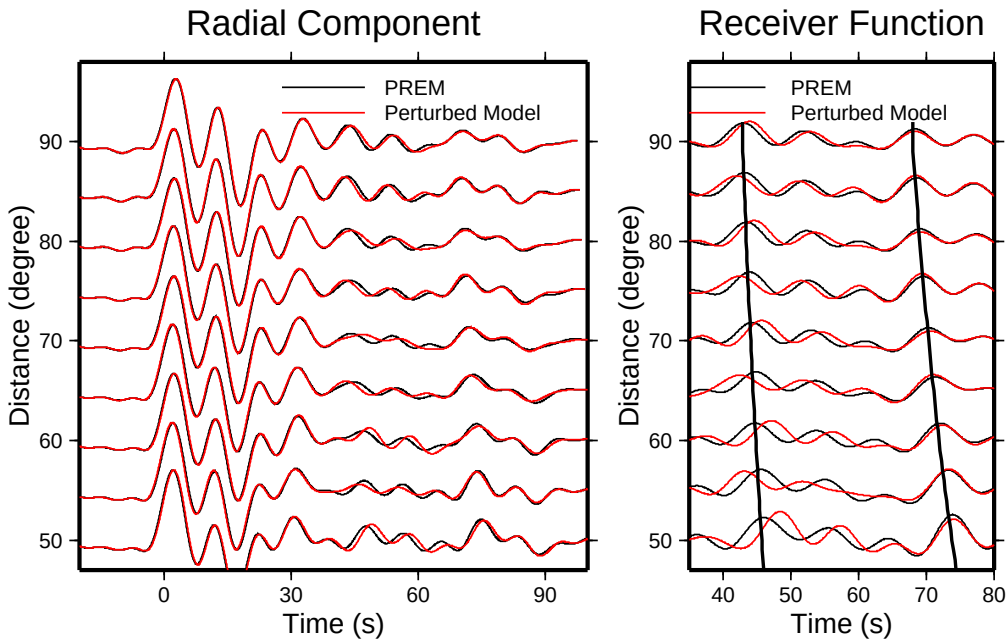

Figure 2.5: (left) Example seismograms and (right) receiver functions for PREM and a perturbed model with topography on the 410-km discontinuity. The topographic variation has the same structure as shown in Fig.2.1. Two black lines indicate theoretical arrival times of the *P410s* and the *P660s* on receiver functions.

spherical harmonics structure and is shown in Fig.2.1. The *P410s* peaks on the receiver function traces as well as the multiples following the *P410s* phases are shifted due to topographic variations. The perturbation at the 410-km discontinuity has a small impact on the arrival times of waves converted at the 660-km discontinuity.

2.2 The 660-km Discontinuity in SEM

Following the implementation of the 410-km discontinuity, we deform the SEM mesh to incorporate topography of the 660-km discontinuity and investigate delay times caused by the topographic variations. Fig.2.6 shows an example SEM mesh with a deformed 660-km discontinuity. A major difference here is that the mesh is doubled in size just below the 660-km discontinuity to maintain a similar number of grid points per seismic wavelength

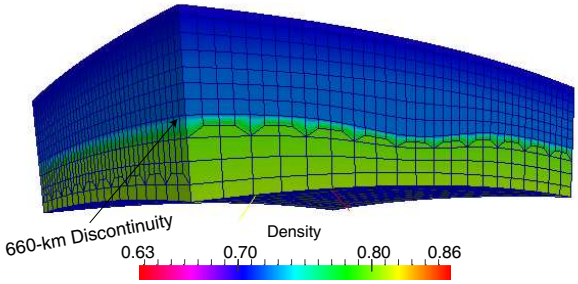

Figure 2.6: Example SEM mesh showing topography of the 660-km discontinuity. The topographic variation has a Gaussian structure. The color scale indicates density normalized by the average value of the Earth $\bar{\rho} = 5514.3$ kg/m^3.

(Komatitsch & Tromp, 2002). Elements have an irregular shape because of the mesh doubling. The accuracy of an SEM simulation can not be guaranteed if the mesh is distorted too much (Komatitsch & Tromp, 2002). This limits topographic variations in both radial and lateral directions. In this paper, the maximum radial perturbation of the 660-km discontinuity is limited to 30 km and the minimum length scale is ∼400 km.

2.3 First-order Seismic Discontinuity

The increases in wavespeeds and densities across the 410-km and 660-km discontinuity result in seismic energy reflection and wave conversion which can be identified in observed seismograms. The sharpness as well as impedance contrast across the discontinuities can provide important constraints to models of upper-mantle thermal and compositional structure. Mineral experimental results show that the impedance "jump" should occur over a finite depth interval as mantle minerals involved in the phase transformation can coexist over a pressure range. The depth range where solid solutions coexist depends on iron content and it can reach tens of kilometers (Ringwood, 1991; Frost, 2008). In addition, not all phase transformations occur in equilibrium and phase transformation may take place very slowly in cold subduction environment (Sung & Burns, 1976). Seismic studies have yielded different

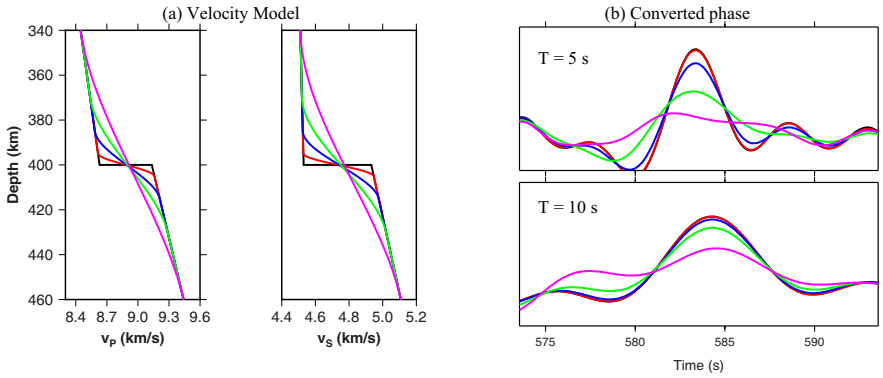

Figure 2.7: (a) Earth models with different structure of the 410-km "discontinuity". The black line shows a first-order discontinuity; red, blue, green and pink lines correspond to "discontinuity" thickness of 10 km, 30 km, 60 km and 120 km, respectively. (b) Corresponding *P-to-S* converted phases on radial-component seismograms.

estimates about the "thickness" of the discontinuities. For example, a broad high-gradient zone extending from 400 to 435 km depth, rather than a sharp first-order discontinuity, was suggested beneath the Siberian platform (Priestley et al., 1994); while high frequency *PP* precursors show the 410-km discontinuity can be as sharp as 4 km beneath the Indian Ocean (Benz & Vidale, 1993).

To investigate the potential of using *P-to-S* scattered waves in determining the sharpness of the transition zone discontinuities, we replace the first-order discontinuity at 400 km depth in PREM with smooth gradient zones of different thickness (Fig.2.7a). In each of the models, the velocity jump at the 410-km discontinuity is replaced by a degree-3 polynomial, which connects smoothly with the reference model at the upper and lower boundary of the gradient zone and preserves the average wavespeed in the depth range. We calculate synthetic seismograms in these models using mode summation and compare *P-to-S* converted phases. Example seismograms at a distance of 50° are shown in Fig.2.7b.

When the wavespeed and density increase occurs over a depth range of tens of kilometers, a clear *S*-phase arrives at the same time as the *P-to-S* converted from a first-order discontinuity as the average wavespeed remains the same regardless of the "thickness" of

the "discontinuity" in the models. The peak becomes wider and amplitude becomes smaller when the depth interval becomes larger. The arrival time of the converted phase can therefore provide reliable constraint on the "equivalent" first-order discontinuity depth while the amplitude is sensitive to the discontinuity structure and can be potentially used to constrain the sharpness of the discontinuity. When the impedance contrast occurs in a very wide depth interval (>100 km), the S-phase becomes much weaker at a period of 10 s and can not be clearly identified at a period of 5 s.

Chapter 3

Receiver Functions

Teleseismic P waves give rise to converted S waves at transition zone discontinuities close to receivers. The converted S waves arrive in the P wave coda and provide important constrains upon the topography of the discontinuities. Receiver functions, which isolate *P-to-S* scattered waves from mantle discontinuities, can be obtained by deconvolving the vertical component seismogram from the radial component, and, its spectra is simply

$$H(\omega) = \frac{R(\omega)}{Z(\omega)}, \tag{3.1}$$

where $H(\omega)$ is the spectra of receiver function, $R(\omega)$ and $Z(\omega)$ are the spectra of radial- and vertical-component seismograms, respectively. A receiver function can be calculated by spectra division or time domain deconvolution (e.g., Clayton & Wiggins, 1976; Ligorria & Ammon, 1999). In this study, we use spectral division,

$$H(\omega) = \frac{R(\omega)Z^*(\omega)}{\max\{Z(\omega)Z^*(\omega)\}, c \cdot \max\{Z(\omega)Z^*(\omega)\}\}}, \tag{3.2}$$

where the asterisk denotes complex conjugate, and a constant (c) is used as "waterlevel" to stabilize division near spectra minima.

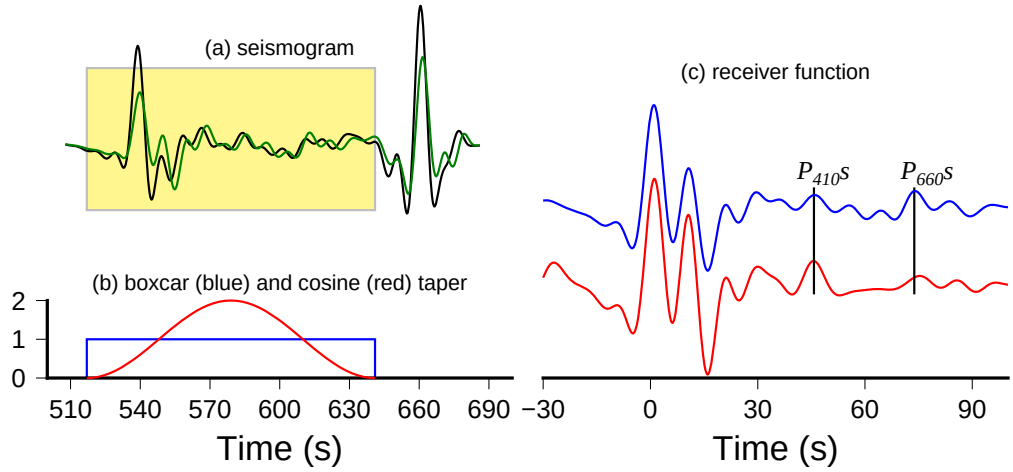

Figure 3.1: Illustration of windowing effects on receiver functions. (a) Simulated vertical (black) and radial (green) component seismograms at an epicentral distance of 50°; the yellow shaded area indicates the portion of the original seismogram used for deconvolution. (b) A boxcar taper (blue) and a cosine taper (red) of the same length as shown in (a). (c) Receiver function calculated using a boxcar taper (blue) and cosine taper (red).

3.1 Effects of Windowing/Tapering

Receiver functions are computed from a portion of observed seismograms following the direct P wave. Windowing and tapering are involved in data processing and they can affect the spectra of calculated receiver functions. For example, a boxcar taper is implicitly used when we cut a portion of the seismogram for analysis. Applying a taper in time domain corresponds to a convolution in frequency domain, and the spectra of a receiver function becomes

$$\tilde{H}(\omega) = \frac{R(\omega) \otimes T(\omega)}{Z(\omega) \otimes T(\omega)}, \tag{3.3}$$

where $R(\omega)$ and $Z(\omega)$ are the spectra of the radial- and vertical-component seismograms, $T(\omega)$ is the spectra of the taper $T(t)$, and the operator $\otimes$ denotes convolution in frequency domain. Fig.3.1 compares receiver functions calculated using a boxcar taper and a cosine taper. Compared to a boxcar taper, a cosine taper enhances signals at center of the time window.

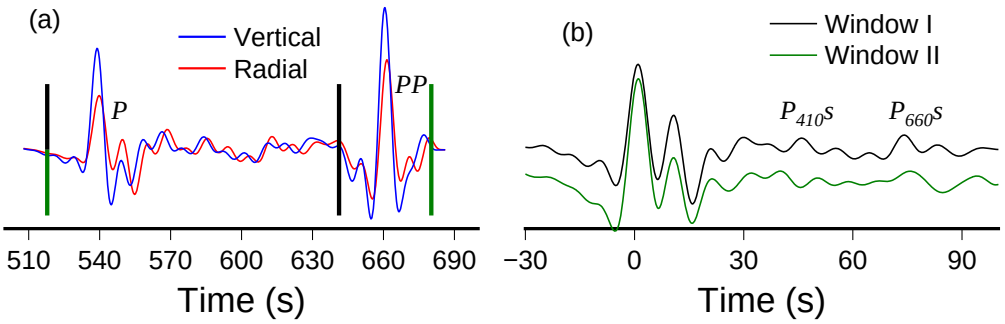

Figure 3.2: Effects of *PP* waves on *P* wave receiver functions. (a) Synthetic vertical and radial component seismograms at an epicentral distance of 50°. (b) Receiver functions calculated using different time windows; window I and II are marked by thick black and green lines in (a), respectively.

3.2 Phase Interactions

The interpretation of receiver functions often assumes coda waves generated by a teleseismic *P* wave. In practice, seismic phases such as surface reflected *PP* waves, core reflected *PcP* waves and depth phase *pP* waves can interfere with direct *P* waves and *P* wave coda. In Fig.3.2, we compare receiver functions calculated using two different measurement windows, with and without *PP* wave included. The calculation shows that including a strong *PP* phase in the deconvolution window will significantly modify phases on the receiver functions, making it difficult to extract useful information from receiver function time series. In the distance range of 30°∼50°, *PP* waves arrive very closely to the *P-to-S* converted waves and excluding *PP* waves from measurement window becomes important.

At epicentral distances of 50°∼60°, *PcP* waves arrive closely to *P-to-S* converted waves from transition zone discontinuities (Fig.3.3). This also violates the assumption that receiver functions from deconvolution represent *P-to-S* conversions from a direct *P* wave. The incident *PcP* waves and *P* waves on the seismic interface have different ray parameters, and receiver function calculated for seismograms with and without strong *PcP* waves show different arrival times associated with transition zone discontinuities. The effects of *PcP* waves

on receiver function delay time measurements will be discussed in Chapter 4.1.

The depth phase, pP waves, can also interfere with P wave coda. For shallow earthquakes, pP waves may be modeled as part of the source process, but strong depth phases from a deep earthquake can heavily influence the spectra of receiver functions and the interaction strongly depend on the depth of the earthquake and epicentral distance (Fig.3.3). In the example shown in Fig.3.3, the depth of the earthquake is 300 km. For this event, the pP wave arrives earlier than the *P660s* wave at distances smaller than 72° and later than the *P660s* wave at larger distances. As a result, the stacked receiver functions show a shallower or deeper 660-km discontinuity depending on the range of epicentral distance of the receiver functions used in stacking.

3.3 Anelasticity in the Reference Model

Seismic waves propagating in the mantle loses its energy due to anelasticity of earth materials. The effects of anelastic attenuation on seismic energy is characterized by the quality factor Q. The inverse of Q is defined as

$$Q^{-1} = \frac{\Delta E}{2\pi E}, \tag{3.4}$$

where E is strain energy and ΔE is energy dissipation per cycle. Higher Q values indicate lower rates of energy loss.

Anelasticity causes wave attenuation as well as physical dispersion. Not much attention has been paid to the effects of physical dispersion in receiver function studies that aim at mapping mantle transition zone discontinuity depths. To investigate effects of anelasticity on receiver functions, we calculate synthetic seismograms in elastic and anelastic earth models and compare calculated receiver functions. In PREM, the bulk quality factor $Q_\kappa = 57827$ in the upper mantle. The effects of anelasticity on P waves are therefore negligible. The quality factor of S waves is much lower in the upper mantle, with $Q_\mu = 80$ between 80 km and 220 km depth and $Q_\mu = 143$ between 220 km and 670 km depth. The low Q values

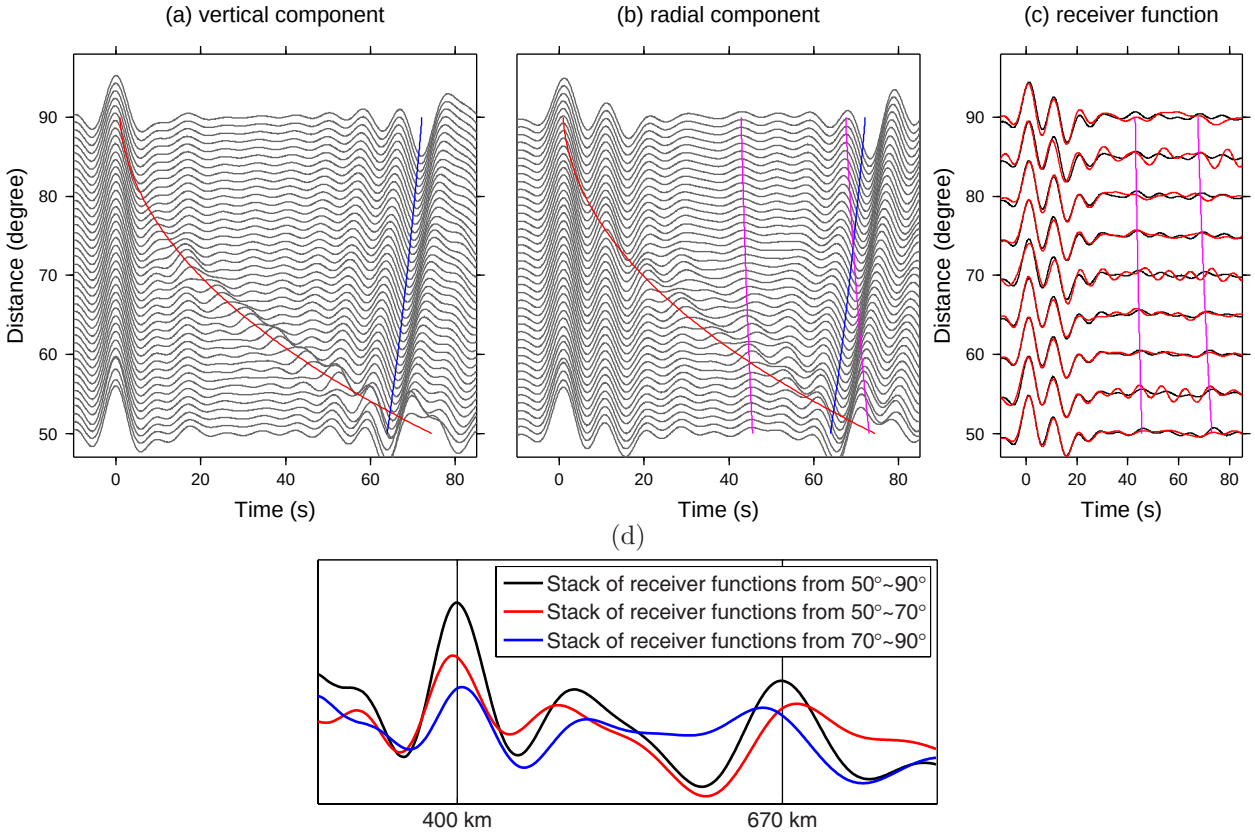

Figure 3.3: Illustration of phase interactions between *P-to-S* waves and *PcP* as well as depth phase *pP* waves. (a and b) Vertical and radial component seismograms at epicentral distances from 50° to 90°. The earthquake is located at 300 km depth. Red and blue lines show theoretical arrival times of core reflected *PcP* and depth phase *pP* waves, respectively. Two pink lines mark the predicted arrival of *P410s* and *P660s* waves. (c) Receiver functions calculated from seismograms generated by a surface source (black) and a deep source at 300 km depth (red). (d) Stacks of receiver functions at different epicentral distance ranges. The *pP* waves arrive earlier than *P660s* wave at distances smaller than ∼72° and later than *P660s* at greater distances for this earthquake.

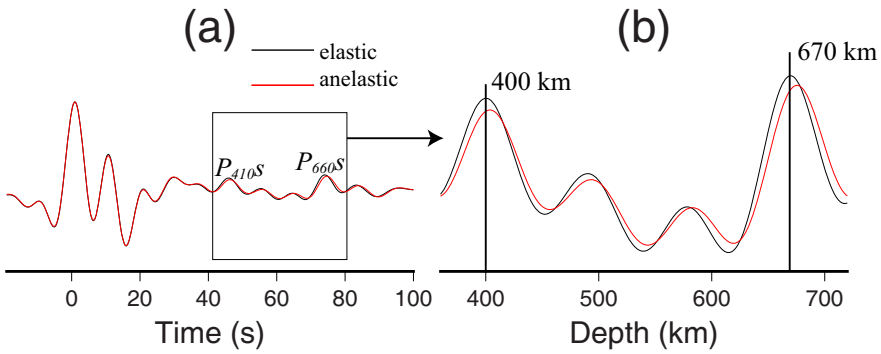

Figure 3.4: (a) Receiver function calculated from synthetic seismograms in purely elastic (black) and anelastic (red) model at an epicentral distance of 50°. (b) Receiver functions mapped to depth.

cause strong physical dispersion as well as amplitude decrease in *P-to-S* converted waves that travel through the upper mantle. The incorporation of anelasticity in the reference model can lead to differences in discontinuity depths by several kilometers when receiver functions are mapped to depth (Fig.3.4). The effects are more significant on *P660s* because the S waves converted at a greater depth travels a longer path. The thickness of the transition zone is less affected as anelasticity introduces time delays in both *P410s* and *P660s* waves.

Physical dispersion can be expressed as

$$c(\omega) = c(\omega_0)\left[1 + \frac{1}{\pi Q}\ln\left(\frac{\omega}{\omega_0}\right)\right], \tag{3.5}$$

where $c(\omega)$ is the seismic wavespeed at angular frequency ω and ω_0 is the reference frequency. Wavespeeds in PREM are often specified at a reference frequency of 1 Hz. If we use an average shear quality factor $Q_\mu = 110$ between 80 km and 670 km depth in the upper mantle, the fractional perturbation in shear velocity caused by anelasticity at a period of 10 s is about -0.67%. For an upgoing *P-to-S* converted wave with an incidence angle close to vertical, the delay times in *P410s* and *P660s* waves at this period are 0.4s and 0.8s, respectively, assuming an average S wavespeed of 5 km/s. This corresponds to about 4 km and 8 km differences in discontinuity depth at the 410- and 660-km discontinuities. The differences will be greater at longer periods. Physical dispersion causes notable decreases in shear velocity at periods longer than 10 seconds, ignoring the effects of anelasticity could lead to biased transition

zone discontinuity depth.

Chapter 4

Finite-Frequency Effects of Receiver Functions

In this chapter, we simulate wave propagation in a range of transition zone discontinuity topographic models, and measure delay times caused by discontinuity perturbations on direct P waves and receiver functions. The frequency-dependent time delay measurements are made on P wave and receiver function seismograms using a transfer function (e.g. Laske & Masters, 1996; Zhou et al., 2006; Kennett & Fichtner, 2012),

$$F(\omega) = \frac{s(\omega)}{s_0(\omega)} = \frac{A(\omega)e^{-i\omega T(\omega)}}{A_0(\omega)e^{-i\omega T_0(\omega)}}. \tag{4.1}$$

Where $F(\omega)$ is the transfer function, $s(\omega)$ is the spectra of tapered seismogram in the perturbed model and $s_0(\omega)$ is the spectra of the seismogram in the reference model. $T(\omega)$ and $T_0(\omega)$ are frequency dependent travel times. In the limit of infinite high frequency, $\omega \to \infty$, T_0 becomes the ray-theoretical traveltime along the ray path (Dahlen & Tromp, 1998). The traveltime anomaly δT can be estimated from the logarithm of the transfer function,

$$\delta T = T - T_0 = -\omega^{-1}\mathrm{Im}\{\ln F(\omega)\}. \tag{4.2}$$

We investigate how delay times vary with wave frequency for each topographic model and discuss wavefront healing effects in P waves as well as receiver functions. Two types of

topographic models are used: models with a spherical harmonics structure and models with a Gaussian structure.

4.1 Topography with Spherical Harmonics Structure

In Fig.4.1, topographic variations of the 410-km discontinuity have a spherical harmonics structure. Topographic models have different length scales in the source-receiver great circle direction and a very long length scale (>1000 km) in the direction perpendicular to ray path. The earthquake is located on the free surface at (0° E, 0° N) and 201 receivers with a 0.2° spacing are located on the equator from 50° E to 90° E to record displacement in wave propagation simulations. Seismograms are windowed to exclude *PP* waves. Receiver functions are calculated using waterlevel deconvolution with a cosine taper applied in spectra estimates, as described in Chapter 3.

In the case where the topographic variation has a length scale of about 2000 km, measured delay times on direct *P* waves at both 20 s and 12.5 s periods agree well with ray predictions. As the wavelength decreases to 1000 km, wavefront healing effects become appreciable at short epicentral distances. The effects become significant when the topography wavelength is about 500 km: at epicentral distances of 50°∼60°, arrival time anomaly of direct *P* waves is ∼50% of ray theory predictions at 12.5 seconds period and ∼30% at 20 seconds period. The arrival anomaly is closer to ray prediction at longer distances. In the case where the wavelength of the 410-km discontinuity topography is about 350 km, measured delay times on direct *P* waves show dramatic differences from ray theory predictions. At 20 seconds period, measurements and ray theory predictions are completely out of phase and measured travel times are several times smaller than ray theory predictions, especially at large epicentral distances. For an actual *P-to-S* conversion occurs at a topographic peak, ray theory predicts a conversion at a neighboring trough. The 12.5 seconds *P*-wave measurements also show a large phase difference from ray theoretical predictions at distances of 50°∼60°. At large epicentral

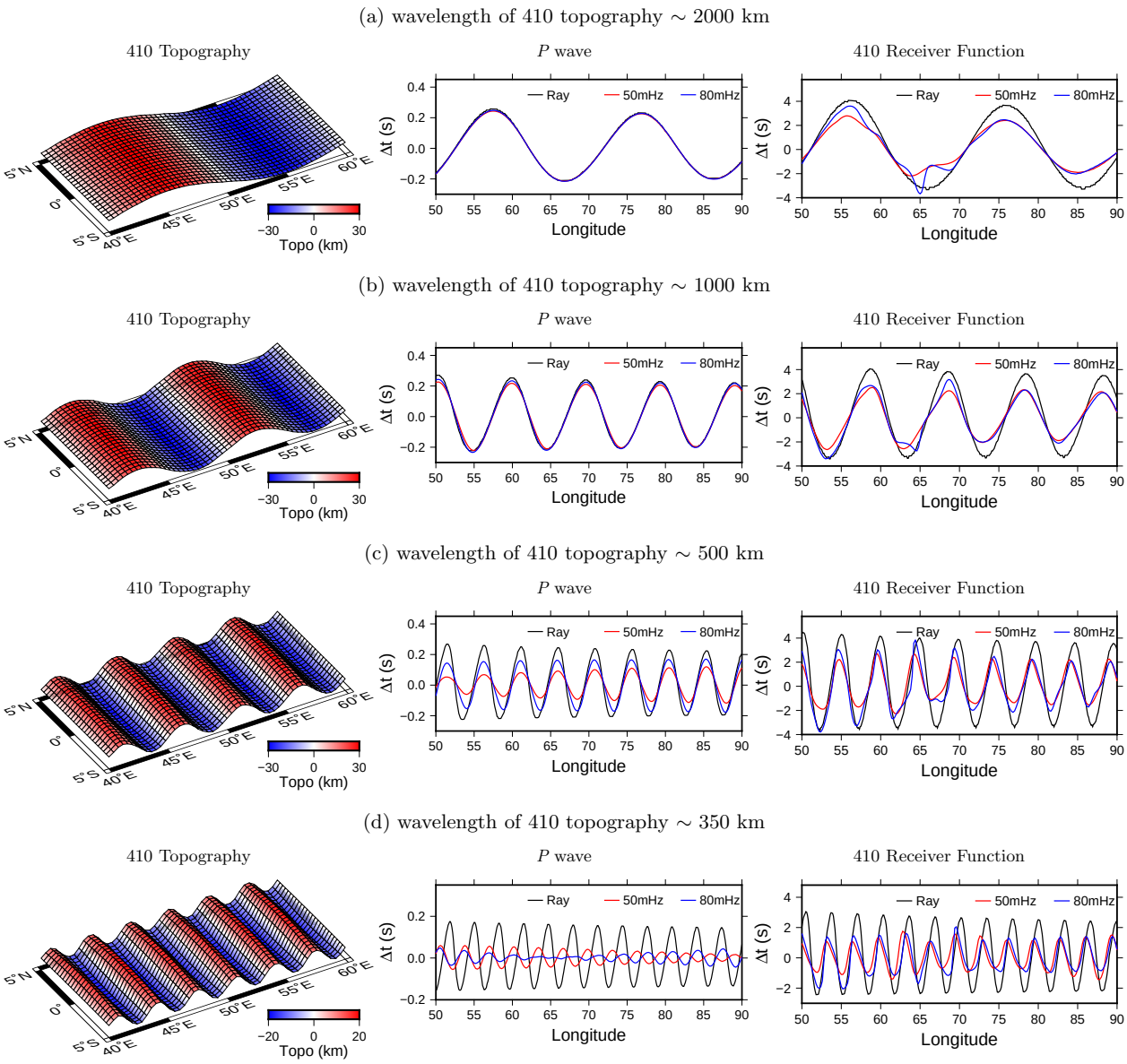

Figure 4.1: Time delays of P waves and *P410s* waves caused by topographic variations at the 410-km discontinuity. The earthquake is located at (0° E, 0° N) and all stations are on the equator. The wavelength of the 410-km discontinuity topography changes from ~2000 km to ~350 km from (a) to (d). Left: the 410-km discontinuity topography on a map view; positive values are upward deflections and negative values are downward deflections. The topographic variation extends from 30° E to 120° E. Middle: comparison of P wave time delays calculated based on ray theory and SEM measurements at 50 mHz (20 s) and 80 mHz (12.5 s). Horizontal axis is station longitude. Right: the same as the middle panel, but for receiver functions.

distances, the 12.5-second (80 mHz) measurements are in phase with ray predictions while the arrival anomaly is only about 30% of predictions based on ray theory.

The measured delays on the *P410s* phase in receiver functions show a complex variation in the spherical harmonics models. When the wavelength of the topography is ∼2000 km, arrival time anomalies are 60∼80% of ray predictions for stations at epicentral distances of 50°∼60°. For stations at distances of 60°∼70°, measurements are affected by strong interactions between *P410s* wave and *PcP* wave because they arrive closely in time, which can not be modeled by predictions based on ray theory as the arrivals at an infinite high frequency do not interfere with each other. At larger epicentral distances of 70°∼90°, measurements do not show strong frequency dependence, and arrival anomalies are about 70% of ray predictions.

As the topography length scale decreases to about 1000 km, the effects of *PcP* waves become weaker and the arrival time anomaly is about 60% of ray predictions. When topography length scale reduces to 300∼500 km, wavefront healing effects become more significant, but in general they are not as strong as in direct *P* waves. The arrival anomaly is about 50% of what predicted by ray theory. Measurements and ray predictions are slightly out of phase as *P-to-S* converted waves "feel" topographic variations in a much larger region than the ray-theoretical conversion point.

4.2 Topography with Gaussian Structure

In theory, any structure on a sphere can be decomposed into spherical harmonics which are basis functions independent of each other. While this allows us to make investigations on the scale dependence in finite-frequency, boundary perturbations often do not have a single periodical structure in tomographic models. This is understood as thermal anomalies introduced by mantle convection (such as subduction slabs) are not periodical features. In this section, we simulate wave propagation in 3-D models where topographies of transition

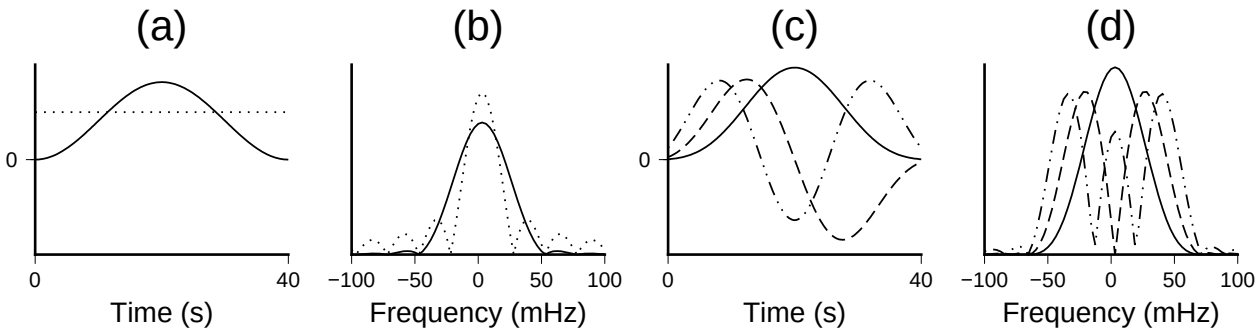

Figure 4.2: (a) Example cosine taper (solid line) and boxcar taper (dotted line) in time domain. (b) Amplitude spectra of the two tapers shown in (a). (c) Example first three 1.5π prolate spheroidal eigentapers. (d) Amplitude of the multitapers in (c).

zone discontinuities have a Gaussian structure, and we measure frequency-dependent arrival times on P waves and receiver functions.

Time delay measurements depend on time-domain tapers used in making the measurements. In Fig.4.2, we plot examples of cosine taper, boxcar taper and first three 1.5π prolate spheroidal multitapers as well as their spectral amplitudes. The boxcar taper has a narrow spectral peak but large side lobes. The spectrum of the cosine taper has very weak side lobes but a broader central peak. The three 1.5π eigentapers are orthogonal to each other and have their spectral energy mostly confined in a frequency band (-62.5, 62.5) mHz for the 40-s time window. We experimented with different tapers in making delay time measurements and found cosine tapers are most reliable for P-wave and receiver function dispersion measurements.

4.2.1 The 410-km discontinuity

In Fig.4.3, we plot P-wave and receiver function delay times measured using a cosine taper for a simple topographic structure of the 410-km discontinuity. The topographic variation of the 410-km discontinuity has a Gaussian structure and the peak perturbation is 30 km. The seismic source is located at (0° E, 0° N) and a number of receivers with a 0.2° spacing

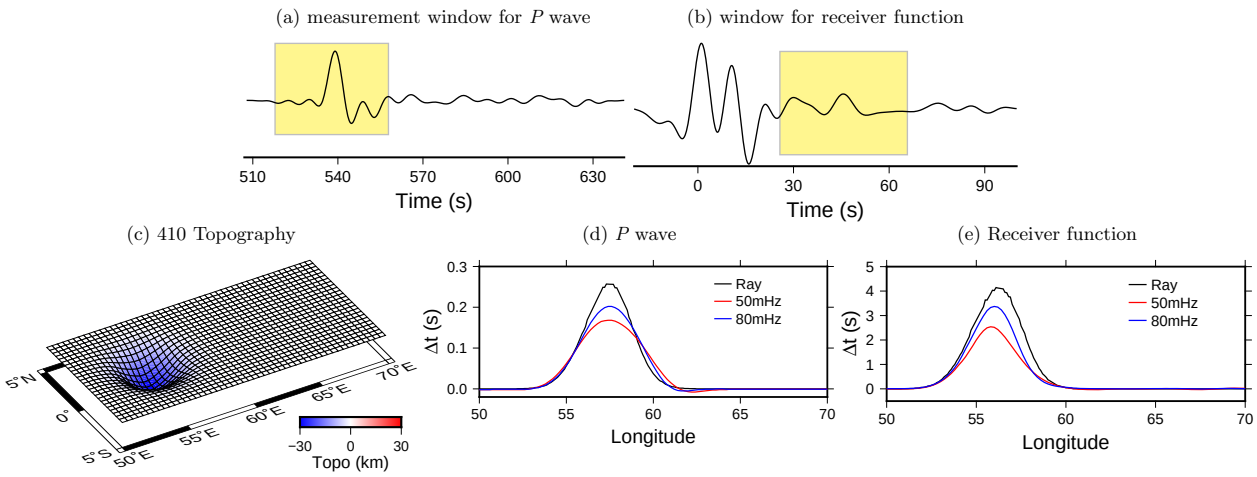

Figure 4.3: (a) Measurement window for direct P wave; it is a 40-second window centered on the P wave arrival. (b) Measurement window of 410 receiver functions; the window length is 40 s and it is centered on the *P410s* phase. (c) The 410-km discontinuity topography on a map view. The topographic variation has a Gaussian structure with a width of ∼800 km. Negative values denote downward deflection of the discontinuity. (d) Time delay measurements made on direct P waves and ray-theoretical predictions. Measurements are made at 50 mHz and 80 mHz using cosine taper. (e) The same as (d), but for receiver functions.

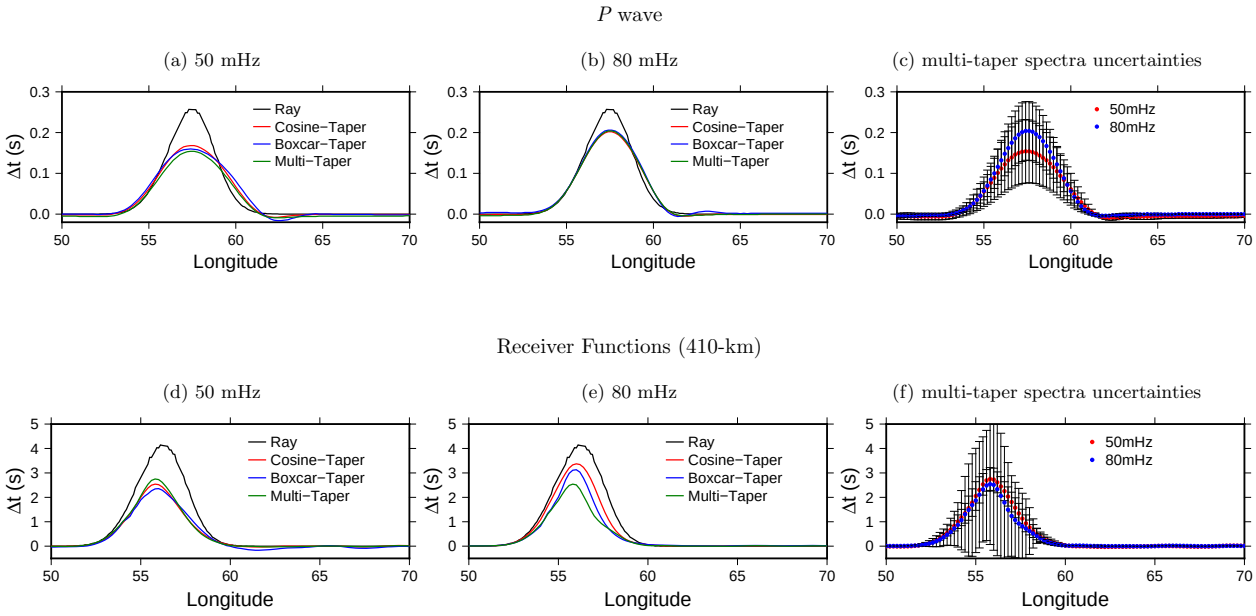

Figure 4.4: Travel time anomalies measured using different tapers. Ray-theoretical predictions are plotted for reference. (a)-(b) are P wave delays measured at 50 mHz and 80 mHz using cosine taper, boxcar taper and multitaper. Spectra uncertainties associated with multitaper measurements are plotted in (c). (d)-(f) are the same as (a)-(c) but for the 410-km discontinuity receiver functions.

are located along the equator from 50° E to 70° E. The comparison between ray-theoretical predictions and cosine taper measurements shows a frequency dependent wavefront healing effects. The arrival anomaly is ∼80% of ray predictions at 12.5-second period (80 mHz) and reduces to ∼65% at 20-second period (50 mHz) for both direct P waves and receiver functions.

We compare measurements made using a cosine taper, boxcar taper and Slepian multitapers (Thomson, 1982) in Fig.4.4. In general, the three techniques give very similar time delay measurements on P waves while the differences are greater in receiver function time delays. The differences arise because the tapers extract different spectral information from the seismograms.

To understand the significance of wavefront healing in receiver functions in imaging topographic variations, we convert the 410-km receiver function time delays to discontinuity

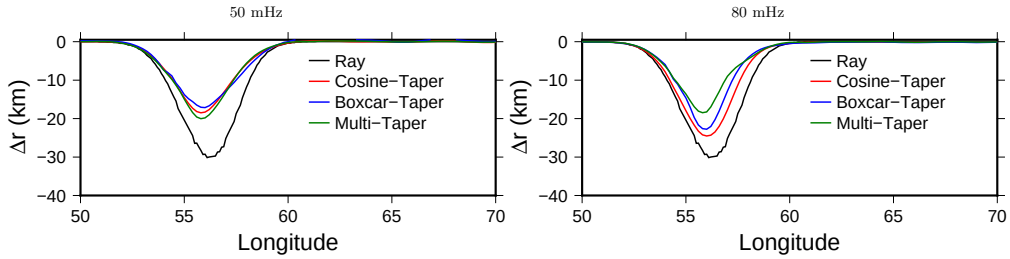

Figure 4.5: Measured delay times in receiver functions in Fig.4.4 are converted to 410-km discontinuity topography.

topography following a simple linear relation between time and depth perturbation in Fig.4.5. While the input peak topography is 30 km, the recovered topography is about 18 km at 20-seconds period and 18-24 km at 12.5-seconds period, depending on measurement techniques.

Finite-frequency effects become more significant when the 410-km discontinuity topography has a shorter length scale. In Fig.4.6, we compare measurements of direct P waves and receiver functions caused by a single downward deflection of the discontinuity with different length scales. When the length scale of the 410-km discontinuity topography is about 400 km, arrival anomaly of the direct P wave is only 20∼30% of ray predictions at periods between 12.5 to 20 seconds. Measured delay times show a broader peak than ray prediction as stations farther away from the topography perturbations also "feel" the anomaly. The effects of wavefront healing are not as strong in receiver functions. The arrival anomaly of the *P410s* wave is about 40%–50% of ray predictions. Measurements and ray predictions are also slightly out of phase as seen in the experiment on spherical harmonics perturbations.

As the length scale further decreases to about 200 km (Fig.4.6c), wavefront healing becomes very strong for both P and *P410s* waves. P waves can hardly "see" such a small-scale topographic variation. The arrival anomaly of the *P410s* wave is only 10∼20% of ray prediction at a 12.5∼20 seconds period and measurements are more out of phase with ray-theoretical predictions.

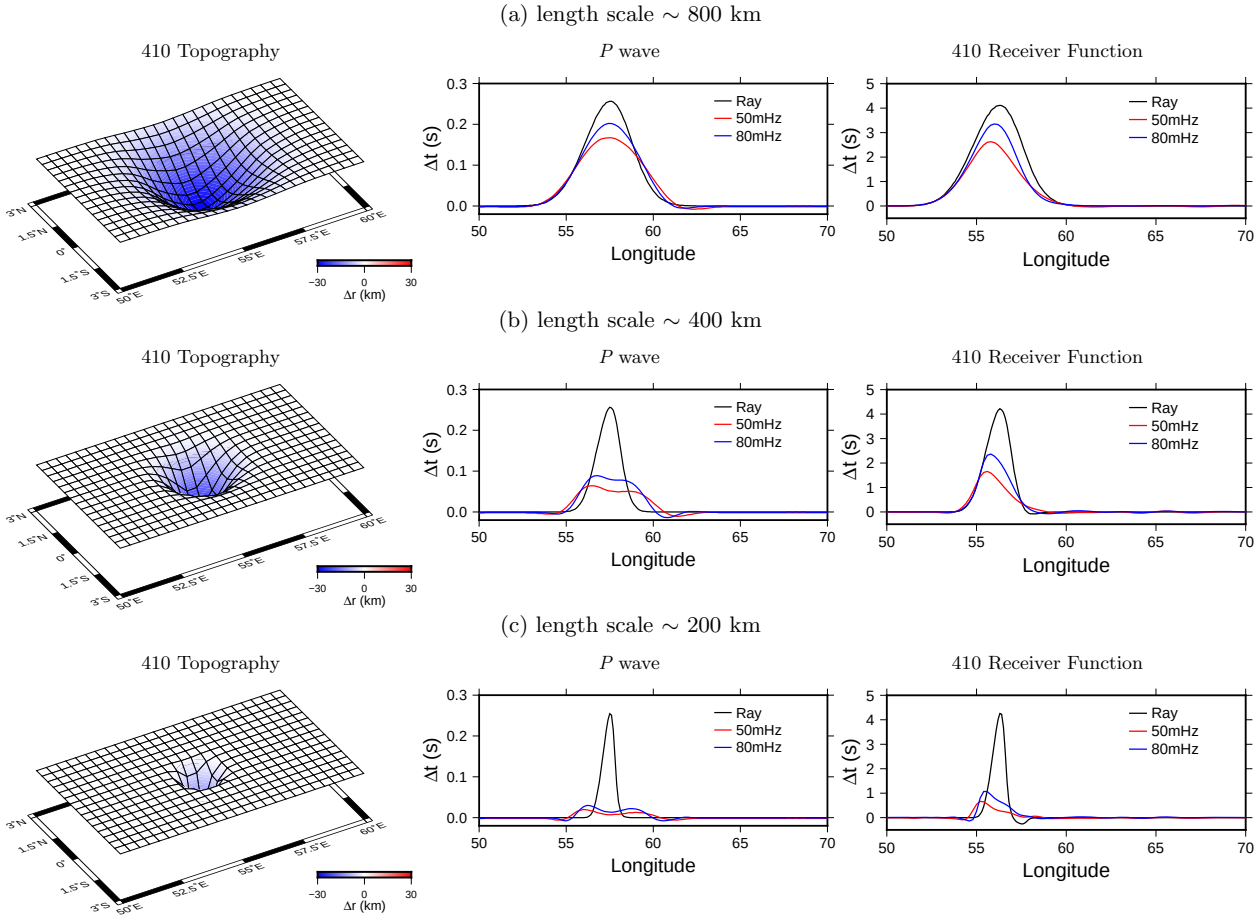

Figure 4.6: Time delays of P waves and *P410s* receiver functions caused by a single downward deflection of the 410-km discontinuity. The 410 topography has a Gaussian structure in both horizontal directions. Length scales of the topography are about 800 km, 400 km and 200 km at the discontinuity in (a), (b) and (c), respectively. The seismic source is located at the free surface at (0° E, 0° N), and receivers are located along the equator from 50° E to 70° E with a 0.2° spacing. Left: The 410-km discontinuity topography on a map view, the peak perturbation is 30 km. Middle: P wave time delays. Right: time delay of the *P410s* phase on receiver functions.

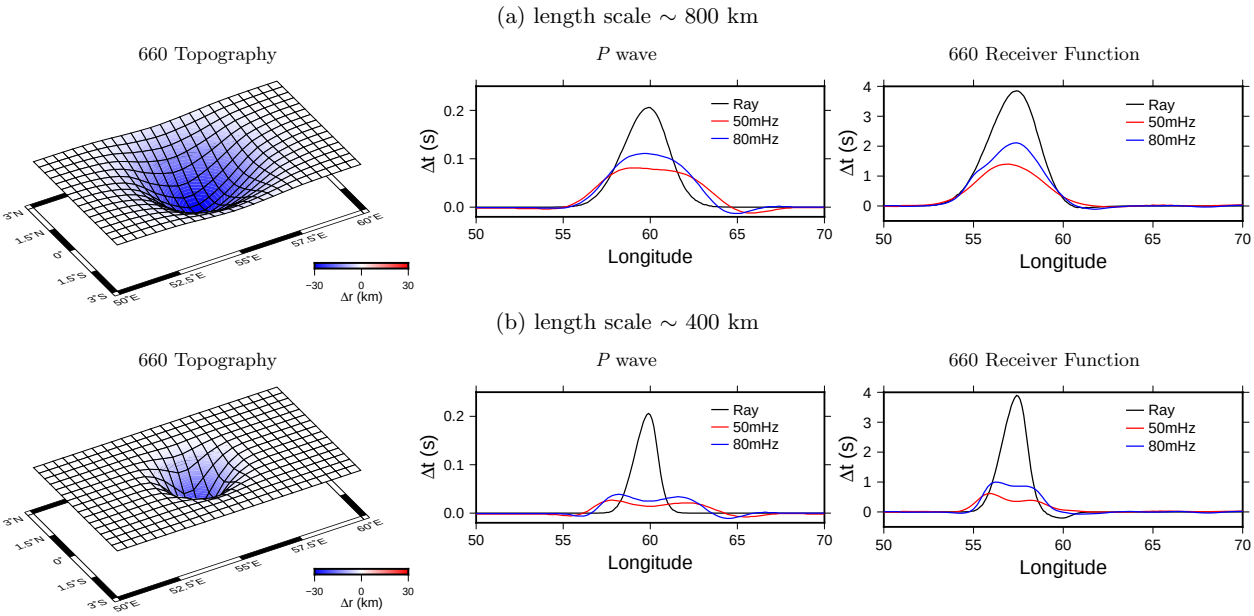

Figure 4.7: The same as Fig.4.6 but for topography at the 660-km discontinuity.

4.2.2 The 660-km Discontinuity

Topographic variations of the 660-km discontinuity and associated travel time measurements for P waves and *P660s* waves on receiver functions are shown in Fig.4.7. Our discussion is restricted to topographic variations of length scales greater than 400 km for due to limitations in numerical accuracy discussed in Chapter 2.2.

When the length scale of the 660-km discontinuity topography is about 800 km (Fig.4.7a), measured arrival time anomaly is 50∼60% of ray-theoretical predictions at a frequency of 50∼80 mHz (12.5-20 s period) for both P waves and *P660s* phase on receiver functions. The *P660s* waves on receiver functions are affected by interaction between *PcP* and *P660s* waves in the measurement window at around 55°.

For smaller scale perturbations of ∼400 km (Fig.4.7b), travel time anomalies of P waves are about 15% of ray-theoretical predictions and the measurements show a almost twice broader distance range where stations "feel" the topographic perturbations. In this case, delay times of *P660s* phases on receiver functions measured at 50 mHz and 80 mHz are only

about 20∼30% of what predicted based on ray theory.

By comparing Fig.4.6 and Fig.4.7, we see direct P waves and receiver functions have different sensitivity to perturbations on the 410-km and 660-km discontinuities. For same length scale topographic variations on the two discontinuities, wavefront healing is much stronger for perturbations on the 660-km discontinuity.

4.3 Finite-Frequency Sensitivity

Our numerical simulations show that finite-frequency effects become important when the length scale of topographic perturbations is smaller or comparable to the size of the Fresnel zone. In this section, we explore finite-frequency Born sensitivity kernels in accounting for wave diffraction effects at the 410-km and 660-km discontinuities in direct P waves as well as in receiver functions.

We calculate boundary sensitivity kernels for phase delays measured between synthetic and observed seismograms based on surface-wave mode summation which is a traveling wave representation of normal modes. The 2-D sensitivity of P-wave to perturbations in discontinuity depths are calculated using the boundary sensitivity kernels in an isotropic reference earth model (Zhou et al., 2005), where a phase delay can be written as

$$\delta\phi(\omega) = \iint_{\Sigma} K_{\phi}^{d}(\mathbf{x},\omega)\delta r(\mathbf{x})\,\mathrm{d}\Sigma, \tag{4.3}$$

where $K_{\phi}^{d}(\omega,\mathbf{x})$ is the phase sensitivity kernel, representing the sensitivity of a phase delay at an angular frequency ω to depth perturbations on a discontinuity, and $\delta r(\mathbf{x})$ is the perturbation in discontinuity depth and the integration is over the discontinuity surface Σ in a spherically symmetric reference model. The relation between phase delay $\delta\phi(\omega)$ and time delay $\delta T(\omega)$ in Eq. (4.2) is simply $\delta\phi(\omega) = \omega\,\delta T$.

The phase delay sensitivity kernel K_{ϕ}^{d} can be calculated based on a complex boundary

sensitivity kernel for the displace spectra of scattered waves,

$$\begin{aligned}\mathcal{K}^d(\mathbf{x},\omega) = &\sum_{\sigma'}\sum_{\sigma''}\mathcal{S}'\left[\frac{\mathrm{e}^{-i(k'\Delta'-n'\pi/2+\pi/4)}}{\sqrt{8\pi k'|\sin\Delta'|}}\right] \\ &\times\left[\frac{\mathrm{e}^{-i(k''\Delta''-n''\pi/2+\pi/4)}}{\sqrt{8\pi k''|\sin\Delta''|}}\right]\mathcal{R}'' \\ &\times[\Omega^{(1)}+\Omega^{(2)}]^+_-,\end{aligned} \tag{4.4}$$

and

$$K^d_\phi(\mathbf{x},\omega) = -\mathrm{Im}\left\{\frac{\left[\mathcal{K}^d(\mathbf{x},\omega)\otimes h(\omega)\right]\left[s(\omega)\otimes h(\omega)\right]^*}{\left[s(\omega)\otimes h(\omega)\right]\left[s(\omega)\otimes h(\omega)\right]^*}\right\}. \tag{4.5}$$

The quantity $\mathcal{S}'$ is the source term of the scattered wave and $\mathcal{R}''$ is the receiver term of the scattered wave. k is the reference wavenumber and Δ is source-to-receiver great-circle distance. The integer n is the polar-passage index. The single and double primes indicate quantities associated with scattered waves from source to scatter (mode σ') and from scatter to receiver (mode σ''), respectively. Expressions of the source term, receiver term and scattering coefficients $\Omega^{(1)}$ and $\Omega^{(2)}$ can be found in Zhou et al. (2005). $h(\omega)$ is the spectrum of the cosine taper used in measurements and $s(\omega)\otimes h(\omega)$ is the spectrum of the tapered reference waveform.

Example 2-D boundary sensitivity kernels for P waves phase delays are plotted in Fig.4.8. P waves have a much broader and weaker first Fresnel zone at the 660-km discontinuity than at the 410-km discontinuity, resulting stronger wavefront healing effects in delay time measurements. P waves traveling through topographic variation on the 660-km discontinuity will experience stronger wavefront healing than that traveling through a similar structure on the 410-km discontinuity.

We compare time delay measurements with calculations based upon ray theory and boundary sensitivity kernels at 50 mHz in Figures 4.9 and 4.10. While ray theory over predicts the delay times of P waves, wavefront healing effects of direct P waves can be properly accounted for by the 2-D boundary sensitivity kernels. This indicates that the relation between travel time anomalies and 410-km and 660-km discontinuity depth perturbations

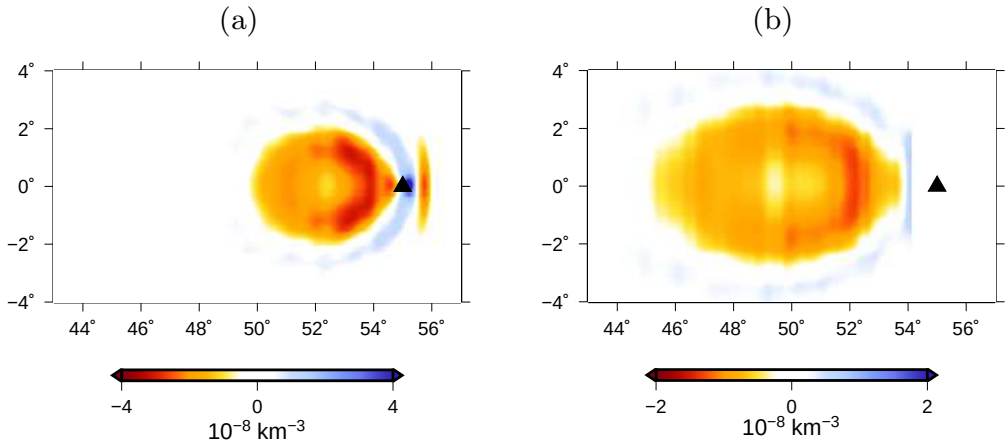

Figure 4.8: Example 2-D boundary sensitivity of P waves to topographic perturbations at the 410-km discontinuity (a) and the 660-km discontinuity (b). The epicentral distance is 55° and the location of the receiver is indicated by a triangle. The sensitivity kernels are calculated for cosine taper delay time measurements. The sensitivity is negative in the first Fresnel zone, indicating an uplifted discontinuity will result in negative phase delays.

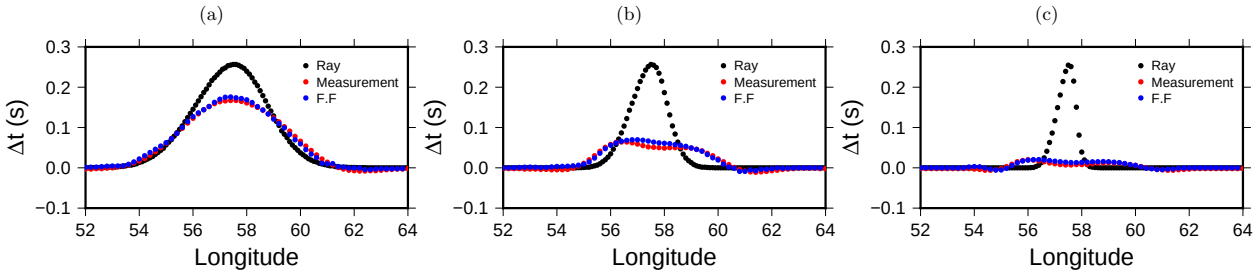

Figure 4.9: P wave travel time measurements at 50 mHz as well as calculations based on ray theory (Ray) and boundary finite-frequency sensitivity kernels (F.F). (a), (b) and (c) correspond to topographic models in Fig.4.6 (a), (b) and (c), respectively.

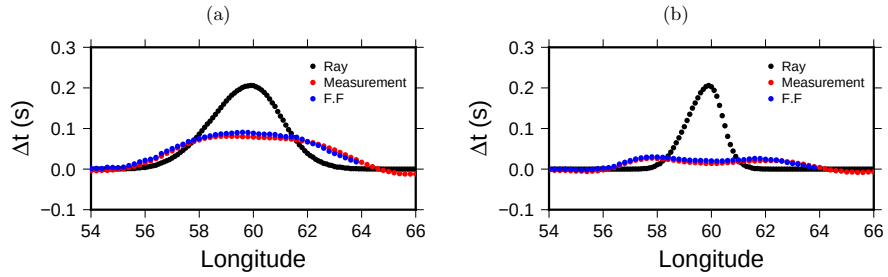

Figure 4.10: P wave travel time measurements at 50 mHz as well as calculations based on ray theory (Ray) and boundary finite-frequency sensitivity kernels (F.F). (a) and (b) correspond to topographic models in Fig.4.7 (a) and (b), respectively.

is close to linear for large topographic variations (up to 30 km). A linear relation between cross-correlation delay times and velocity anomalies for large wave speed perturbations (up to 10%) was also suggested (Mercerat & Nolet, 2013).

In Fig. 4.11, we calculate the finite-frequency sensitivity of receiver functions to perturbations in discontinuity depth. The receiver function sensitivities are formulated for topographic perturbations based on surface-wave mode coupling (Deng & Zhou, in prep). While the *P410s* phase on receiver functions emphasize differences in arrival time between direct P and *P410s* waves, the size of the Fresnel zone in Fig. 4.11 is smaller compared to P wave sensitivity, but close to the Fresnel zone of the *P410s* wave (Figs A.1 and A.2). This is consistent with measurements made on SEM seismograms which show stronger healing effects on P waves than in receiver functions. The delay time measurements can be reasonably recovered using 2-D boundary sensitivity kernels for receiver functions.

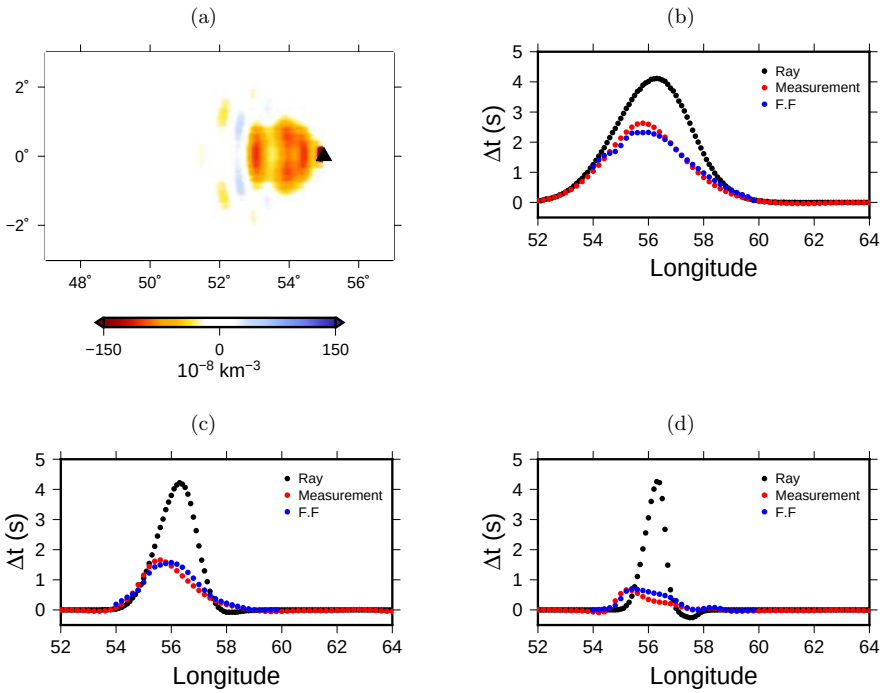

Figure 4.11: (a) Example 2-D boundary sensitivity of receiver functions to topographic perturbations at the 410-km discontinuity. The epicentral distance is 55° and the location of the receiver is indicated by a triangle. The sensitivities are calculated for a cosine taper time delay measurement made on receiver functions. (b)-(d) Receiver function travel time measurements at 50 mHz as well as predictions based on ray theory (Ray) and finite-frequency boundary sensitivity kernels (F.F). (b), (c) and (d) correspond to topographic models in Fig.4.6 (a), (b) and (c), respectively.

Chapter 5

Tradeoff Between 3-D Wavespeed Structure and Discontinuity Depth

Receiver functions are usually mapped to depth following the arrival time of a *Pds* phase relative to direct P wave in a spherical earth,

$$T_{P_ds} = \int_{R_d}^{R_0} \left(\sqrt{\frac{r^2}{v_s^2} - p_{P_ds}^2} - \sqrt{\frac{r^2}{v_p^2} - p_P^2} \right) \frac{\mathrm{d}r}{r}, \tag{5.1}$$

where R_0 is the Earth radius, R_d is the radius of the discontinuity, v_s and v_p are S and P wavespeeds, and p_P and p_{P_ds} are the spherical ray parameters of P waves and *P-to-S* converted waves. To map the depths of transition zone discontinuities, corrections for wavespeed anomalies in the mantle are necessary when lateral wavespeed heterogeneities are present near receivers. It has been pointed out that time corrections based on regional P and S tomographic structure reduce the standard deviations of 410 and 660 depths and provide more reliable upper mantle discontinuity structures (Eagar et al., 2010; Schmandt et al., 2012). While velocity corrections based on ray theory only account for wavespeed structure along seismic ray paths, finite-frequency effects can be important when the size of lateral heterogeneities is comparable to the characteristic seismic wavelength.

To illustrate possible artifacts of discontinuity topography introduced by uncorrected

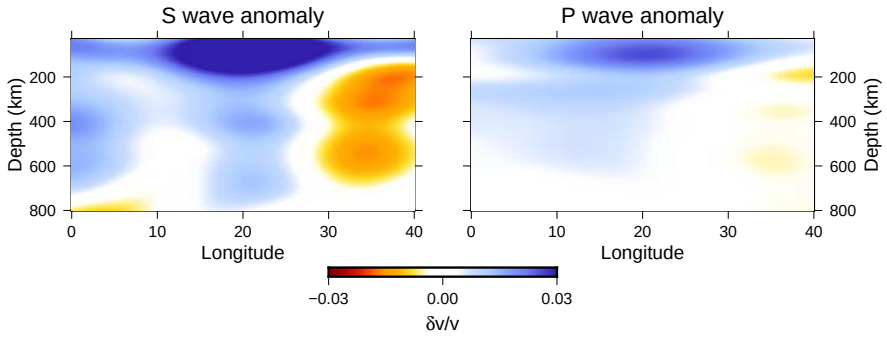

Figure 5.1: A cross section of mantle model S20RTS (Ritsema et al., 1999) beneath stations in our simulation. Color scale indicates fractional perturbations of S-wave speed (left) and P-wave speed (right) in model S20RTS. The color scale saturates at -3% and +3%.

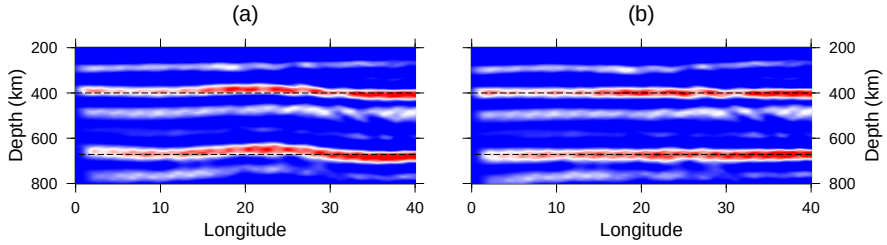

Figure 5.2: Transition zone discontinuity imaged by common conversion point (CCP) stacking of receiver functions (a) with and (b) without wavespeed corrections. Dash lines show the actual depths of the 410-km and 660-km discontinuity. Earth model is PREM+S20RTS.

travel time anomalies caused by 3-D wavespeed structure, we incorporate 3-D mantle model S20RTS (Ritsema et al., 1999) in SEM simulations. S20RTS is a low resolution model with shortest length scale of l=20 ($\sim$900 km in the upper mantle). The transition zone discontinuities at the depths of 400 km and 670 km do not vary in simulations. The seismic source is locate at (90°E, 0°N) and receivers are located along equator from 0°E to 40°E. The SEM receiver functions are first mapped to depth using 1-D reference model PREM. In Fig.5.2a, the common-conversion-point stacking (CCP) of receiver functions shows an artifact of upward deflection of the two discontinuities between 15° and 25° and an artifact of downward deflection between 30° and 40°. Thickness of the transition zone is less affected. The "recovered" topography of the 410-km and 660-km discontinuities are artifacts of ignoring the effects of a fast anomaly in S wavespeed between 15° and 25° in the upper mantle and a slow anomaly between 30° and 40° (Fig.5.1). In Fig.5.2b, we use ray theory to correct for time differences caused by wavespeed anomalies in S20RTS and show that the original depths of the two discontinuities can be recovered.

To investigate finite-frequency effects of 3-D wavespeed structure on receiver functions, we introduce three wavespeed anomalies in SEM simulations and measure time delays in direct P waves as well as in receiver functions. The three anomalies have different lateral sizes and the fractional perturbation of wavespeed is -2% for P wave and -4% for S wave, with respect to PREM. The relative strength of P and S wave anomaly is similar to global upper mantle tomographic models. 51 receivers with a 0.2° spacing are used to record waveforms in each simulation. To avoid artifacts caused by sharp boundary of wavespeed anomalies, perturbations have a Gaussian structure in both horizontal and vertical directions.

P waves and receiver functions both show wave front healing effects when the size of the anomaly is small ($\leq$400 km). When the lateral size of the wavespeed anomaly is about 300 km, the arrival anomaly of P wave is 50% of ray-theoretical predictions at 50 mHz and is about 65% at 80 mHz. The travel time anomaly of the *P410s* phase on receiver functions is about 65$\sim$70% of ray-theoretical predictions at the same frequency. Wavefront healing is stronger for P wave as it has a broader first Fresnel zone than the S phase on

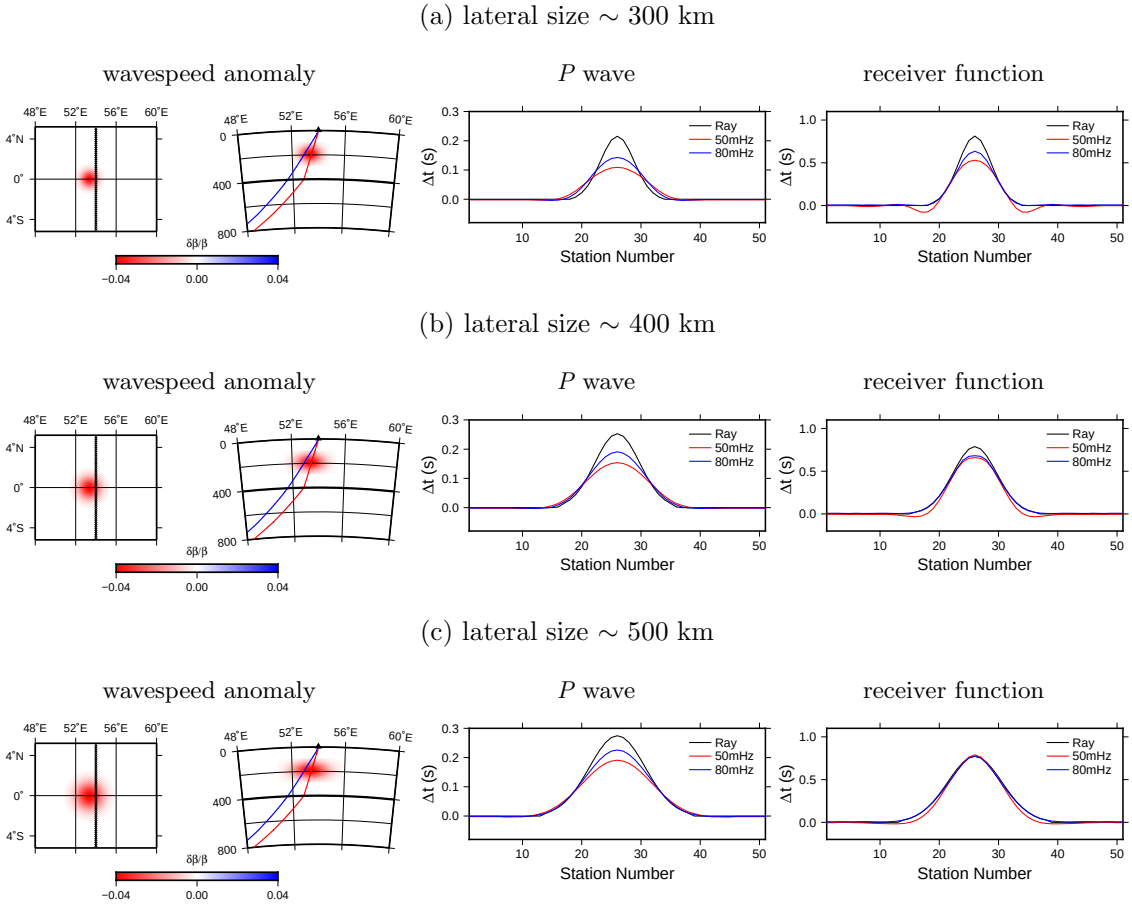

Figure 5.3: Wavespeed anomalies of different sizes and time delays caused by the anomalies. Left: map view and cross section view of the wavespeed anomaly; the color scale indicates fractional perturbation of shear velocity; black triangles show the locations of 51 receivers; blue and red lines show ray paths of *P* waves and *P410s* waves, respectively. Middle: time delay of *P* waves calculated based on ray theory and measurements at 50 mHz and 80 mHz. Right: time delay of the *P410s* phase on receiver functions.

receiver functions at the same period. This can be understood because receiver functions are sensitive to relative arrival of P and *P-to-S* converted waves. Finite-frequency effects in 3-D wavespeed time corrections can be neglected in receiver function migrations when lateral size of wavespeed anomaly is greater than 500 km.

Chapter 6

Conclusion

SEM simulations in a range of transition zone discontinuity topographic models confirm that wave diffractional effects become significant when the length scale of discontinuity topography is smaller or comparable to the size of the Fresnel zone. This is case for both P waves and *P-to-S* converted phases on receiver functions. At a period of 10∼20 seconds, observed travel time of the *P410s* phase on receiver functions is about 50% of ray-theoretical predictions when the length scale of topography at the 410-km discontinuity is about 400 km. The observed travel time anomaly further reduces to 10∼20% or ray-theoretical prediction when topography length scale is about 200 km. Finite-frequency effects are more significant in waves responding to topography at the 660-km discontinuity.

In receiver function migration, travel time anomalies caused by wavespeed structure need to be corrected for. We simulate wave propagation in 3-D wavespeed models and show that finite-frequency effects become important when the length scale of anomalies is less than 500 km. In low resolution tomographic models such as S20RTS (Ritsema et al., 1999), the length scale of wavespeed anomalies exceeds 1000 km and travel time corrections do not show significant finite-frequency effects.

Transition zone phase transformations may occur over a depth range and a first-order

seismic discontinuity may not be present in the transition zone. In the case where wavespeed and density increases occur over a depth range of 30∼60 km, travel time of a *P-to-S* converted phase can be used to find the equivalent first-order discontinuity and their amplitudes could be potentially used to constrain the "thickness" of transition zone discontinuities. We point out that amplitudes of P-to-S converted may also be affected by topography of the discontinuity and lateral variations in anelasticity. Physical dispersion at a period of 10∼20 seconds caused by anelasticity in the upper mantle can introduce several kilometers difference in mapping receiver functions to transition zone discontinuity depths. The thickness of transition zone is less affected because anelasticity causes time delays in both *P410s* and *P660s* waves.

We calculate 2-D finite-frequency sensitivity to discontinuity depth perturbations and show that wave diffraction effects in direct P waves as well as *P-to-S* converted phases on receiver functions can be accounted for. The effects of windowing, tapering, and phase interaction have be fully taken into in the construction of sensitivity kernels. Finite-frequency sensitivity kernels in this paper are calculated based on a first-order Born approximation. We show that calculations based on Born sensitivity kernels fit "ground-truth" measurements very well for large topographic variations (up to 30 km) of the 410-km and 660-km discontinuities. In traditional receiver function analysis where receiver functions at different frequency bands are only used to infer wavelength dependency of seismic discontinuities, finite-frequency sensitivity kernels allow for inversions of first-order discontinuity topography making use of measurements at various frequencies.

Bibliography

Andrews, J. & Deuss, A., 2008. Detailed nature of the 660 km region of the mantle from global receiver function data, *Journal of Geophysical Research-Solid Earth*, **113**(B6).

Benoit, M. H., Long, M. D., & King, S. D., 2013. Anomalously thin transition zone and apparently isotropic upper mantle beneath bermuda: Evidence for upwelling, *Geochemistry, Geophysics, Geosystems*, **14**(10), 4282–4291.

Benz, H. M. & Vidale, J. E., 1993. Sharpness of upper-mantle discontinuities determined from high-frequency reflections, *Nature*, **365**(6442), 147–150.

Bina, C. R. & Helffrich, G., 1994. Phase-transition clapeyron slopes and transition zone seismic discontinuity topography, *Journal of Geophysical Research-Solid Earth*, **99**(B8), 15853–15860.

Birch, F., 1952. Elasticity and constitution of the earth's interior, *Journal of Geophysical Research*, **57**, 227–286.

Cao, A. & Levander, A., 2010. High-resolution transition zone structures of the gorda slab beneath the western united states: Implication for deep water subduction, *Journal of Geophysical Research-Solid Earth*, **115**.

Clayton, R. W. & Wiggins, R. A., 1976. Source shape estimation and deconvolution of teleseismic body-waves, *Geophysical Journal of the Royal Astronomical Society*, **47**(1), 151–177.

Dahlen, F. A., 2005. Finite-frequency sensitivity kernels for boundary topography perturbations, *Geophysical Journal International*, **162**(2), 525–540.

Dahlen, F. A. & Tromp, J., 1998. *Theoretical Global Seismology*, Princeton University Press.

Dueker, K. G. & Sheehan, A. F., 1997. Mantle discontinuity structure from midpoint stacks of converted p to s waves across the yellowstone hotspot track, *Journal of Geophysical Research-Solid Earth*, **102**(B4), 8313–8327.

Dziewonski, A. M. & Anderson, D. L., 1981. Preliminary reference earth model, *Physics of the Earth and Planetary Interiors*, **25**(4), 297–356.

Eagar, K. C., Fouch, M. J., & James, D. E., 2010. Receiver function imaging of upper mantle complexity beneath the pacific northwest, united states, *Earth and Planetary Science Letters*, **297**(1-2), 141–153.

Flanagan, M. & Shearer, P. M., 1998. Topography on the 410-km seismic velocity discontinuity near subduction zones from stacking of ss, sp, and pp precursors, *Journal of Geophysical Research*, **103**, 21,165–21,182.

Frost, D. J., 2008. The upper mantle and transition zone, *Elements*, **4**(3), 171–176.

Helffrich, G., Faria, B., Fonseca, J. F. B. D., Lodge, A., & Kaneshima, S., 2010. Transition zone structure under a stationary hot spot: Cape verde, *Earth and Planetary Science Letters*, **289**(1-2), 156–161.

Katsura, T. & Ito, E., 1989. The system mg_2sio_4-fe_2sio_4 at high pressures and temperatures; precise determination of stabilities of olivine, modified spinel, and spinel, *Journal of Geophysical Research*, **94**, 15,663–16,670.

Kennett, B. L. N. & Fichtner, A., 2012. A unified concept for comparison of seismograms using transfer functions, *Geophysical Journal International*, **191**(3), 1403–1416.

Komatitsch, D. & Tromp, J., 1999. Introduction to the spectral element method for three-dimensional seismic wave propagation, *Geophysical Journal International*, **139**(3), 806–822.

Komatitsch, D. & Tromp, J., 2002. Spectral-element simulations of global seismic wave propagation - i. validation, *Geophysical Journal International*, **149**(2), 390–412.

Langston, C. A., 1979. Structure under mount rainier, washington, inferred from teleseismic body waves, *Journal of Geophysical Research*, **84**(Nb9), 4749–4762.

Laske, G. & Masters, G., 1996. Constraints on global phase velocity maps from long-period polarization data, *Journal of Geophysical Research-Solid Earth*, **101**(B7), 16059–16076.

Lawrence, J. F. & Shearer, P. M., 2006. A global study of transition zone thickness using receiver functions, *Journal of Geophysical Research-Solid Earth*, **111**(B6).

Lawrence, J. F. & Shearer, P. M., 2008. Imaging mantle transition zone thickness with sds-ss finite-frequency sensitivity kernels, *Geophysical Journal International*, **174**(1), 143–158.

Leahy, G. M., 2009. Local variability in the 410-km mantle discontinuity under a hotspot, *Earth and Planetary Science Letters*, **288**(1-2), 158–163.

Li, A., Fischer, K. M., Wysession, M. E., & Clarke, T. J., 1998. Mantle discontinuities and temperature under the north american continental keel, *Nature*, **395**, 160163.

Li, X. Q., Kind, R., & Yuan, X. H., 2003. Seismic study of upper mantle and transition zone beneath hotspots, *Physics of the Earth and Planetary Interiors*, **136**(1-2), 79–92.

Ligorria, J. P. & Ammon, C. J., 1999. Iterative deconvolution and receiver-function estimation, *Bulletin of the Seismological Society of America*, **89**(5), 1395–1400.

Long, M. D., Benoit, M. H., Chapman, M. C., & King, S. D., 2010. Upper mantle anisotropy and transition zone thickness beneath southeastern north america and implications for mantle dynamics, *Geochemistry Geophysics Geosystems*, **11**.

Mercerat, E. D. & Nolet, G., 2013. On the linearity of cross-correlation delay times in finite-frequency tomography, *Geophysical Journal Internation*, **192**, 681–687.

Priestley, K., Cipar, J., Egorkin, A., & Pavlenkova, N., 1994. Upper-mantle velocity structure beneath the siberian platform, *Geophysical Journal International*, **118**(2), 369–378.

Ringwood, A. E., 1991. Phase transformation and their bearings on the constitution and dynamics of the mantle, *Geochimica et Cosmochimica Acta*, **55**, 2083–2110.

Ritsema, J., van Heijst, H. J., & Woodhouse, J. H., 1999. Complex shear wave velocity structure imaged beneath africa and iceland, *Science*, **286**(5446), 1925–1928.

Schmandt, B., Dueker, K., Humphreys, E., & Hansen, S., 2012. Hot mantle upwelling across the 660 beneath yellowstone, *Earth and Planetary Science Letters*, **331**, 224–236.

Shearer, P. M. & Masters, T. G., 1992. Global mapping of topography on the 660-km discontinuity, *Nature*, **355**, 791795.

Sheehan, A. F., Shearer, P. M., Gilbert, H. J., & Dueker, K. G., 2000. Seismic migration processing of p-sv converted phases for mantle discontinuity structure beneath the snake river plain, western united states, *Journal of Geophysical Research-Solid Earth*, **105**(B8), 19055–19065.

Sung, C. M. & Burns, R. G., 1976. Kinetics of high-pressure phase transformations: Implications to the evolution of the olivine-spinel transition in the downgoing lithosphere and its consequences on the dynamics of the mantle, *Tectonophysics*, **31**, 1–31.

Thomson, D. J., 1982. Spectrum estimation and harmonic-analysis, *Proceedings of the Ieee*, **70**(9), 1055–1096.

Zhou, Y., 2009. Multimode surface wave sensitivity kernels in radially anisotropic earth media, *Geophysical Journal International*, **176**(3), 865–888.

Zhou, Y., Dahlen, F. A., Nolet, G., & Laske, G., 2005. Finite-frequency effects in global surface-wave tomography, *Geophysical Journal International*, **163**(3), 1087–1111.

Zhou, Y., Nolet, G., Dahlen, F. A., & Laske, G., 2006. Global upper-mantle structure from finite-frequency surface-wave tomography, *Journal of Geophysical Research-Solid Earth*, **111**(B4).

Appendix A

Fresnel Zone of *P* and *P410s* waves

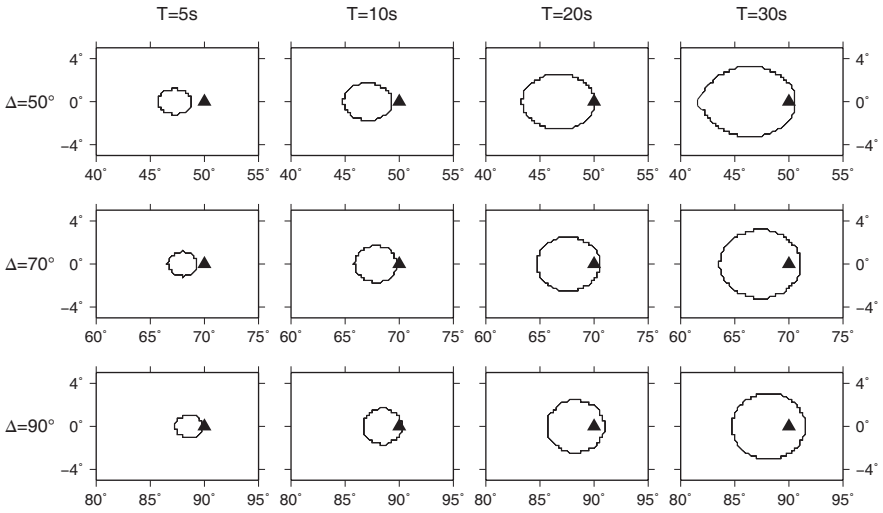

Figure A.1: Fresnel zone of P waves at the 410-km discontinuity.

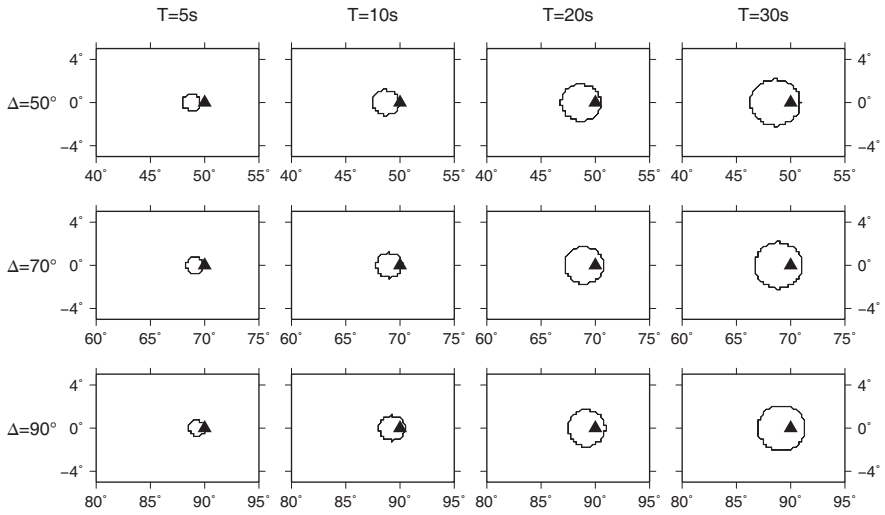

Figure A.2: Fresnel zone of *P410s* waves at the 410-km discontinuity.